

Impacts of Hurricane Irma (2017) on ocean transport processes

Thomas Dobbelaere^{a,*}, Milan Curcic^b, Matthieu le Hénaff^{c,d}, Emmanuel Hanert^{a,e}

^a*Eath and Life Institute (ELI), UCLouvain, Louvain-la-Neuve, Belgium*

^b*Rosenstiel School of Marine and Atmospheric Sciences (RSMAS), University of Miami, Coral Gables, Florida, USA*

^c*Cooperative Institute for Marine and Atmospheric Studies (CIMAS), University of Miami, Miami, Florida, USA*

^d*Atlantic Oceanographic and Meteorological Laboratory (AOML), NOAA, Miami, Florida, USA*

^e*Institute of Mechanics, Materials and Civil Engineering (IMMC), UCLouvain, Louvain-la-Neuve, Belgium*

Abstract

In most hydrodynamic model studies, currents and waves are simulated in an uncoupled manner. These modelled currents can then be used to simulate the trajectories of passive drifters (pollutants, sediments, larvae, etc.) without taking wave or wave-current interactions into account. Although this simplification holds for most situations, as the force exerted by waves on currents can be neglected in fair weather conditions, it may lead to significant errors during storm conditions, when currents are strongly influenced by wind-generated waves. In this study, we investigate current-wave interactions in heavy-wind conditions by coupling the unstructured-mesh hydrodynamic model SLIM with the spectral wave model SWAN. We apply the coupled model in the Florida Reef Tract during Hurricane Irma (Sep. 2017) and show that it successfully reproduces both the observed wave behavior and storm surge during the passage of the hurricane. The modeled currents are then

*Corresponding author

Email address: thomas.dobbelaere@uclouvain.be (Thomas Dobbelaere)

used to simulate the trajectories of passive drifters during the passage of the hurricane. Our results show that taking wave force into account induces variations of up 1 m/s in modelled currents on the continental shelf break as well as in the vicinity of reefs and islands. Wave-current interactions can therefore deflect the trajectories of drifting material by up to 10 km on the passage of the storm **Add something?**. These results strongly advocate for the inclusion of wave forces while studying transport processes (sediments, pollutants, larvae, etc.) in heavy-wind conditions.

Keywords:

1. Introduction

Wave-current interactions in coastal areas are of great importance for coastal engineering as they play a key role in sediment transport, morphological evolution and pollutant mixing (Bever and MacWilliams, 2013; Li and Johns, 1998). However, these interactions are highly nonlinear and can vary significantly in space and time (Wu et al., 2011). Wave-induced currents are generated by wave radiation stress gradients (Longuet-Higgins, 1970), affecting water levels near shorelines and wave breaking points (Longuet-Higgins and Stewart, 1964). Changes in water levels and currents, in turn, affect the motion and evolution of the waves (Sikirić et al., 2013). Coupled wave-current models are therefore required to capture these complex interactions.

As coastal oceans are characterized by complex topology with islands, inlets and estuaries, unstructured (usually two-dimensional) models are preferred as structured grid models show limitations in resolving topologically-controlled nearshore processes (Wu et al., 2011; Chen et al., 2007). Being able to capture the impact of topology on wave interactions becomes even more important in the case of hurricanes. The strong hurricane-induced winds generate large wind-waves and disturb ocean conditions (Liu et al., 2020) by causing coastal upwellings on continental shelves (Smith, 1982) and inducing strong currents, waves and storm surges in nearshore and coastal regions (Dietrich et al., 2010;

21 Weisberg and Zheng, 2006).

22 South Florida and the Gulf of Mexico are particularly vulnerable to
23 hurricanes (Malmstadt et al., 2009) and modelling studies predict tropical
24 cyclones to increase both in frequency and intensity in this region (Marsooli
25 et al., 2019; Knutson et al., 2010). Being able to accurately model wave-current
26 interactions in this area becomes thus critical. *Expand...*

27 Individual-based modelling of particulates has been extensively used to
28 study the transport of drifting materials such as pollutants, sediments or
29 larvae (Le Hénaff et al., 2012; Liubartseva et al., 2018; Figueiredo et al.,
30 2013; Frys et al., 2020). Although some of these studies take the impact of
31 waves into account by adding a Stokes drift velocity, *i.e.* the net drift of a
32 floating particle in the direction of the wave propagation (Van Den Bremer
33 and Breivik, 2018), to the Eulerian currents, they usually neglect the wave-
34 induced currents. Such practice is reasonable in the case of fair weather,
35 when wave-induced forces exerted on currents are relatively small, but might
36 lead to significant inaccuracies during storm conditions (Röhrs et al., 2012;
37 Curcic et al., 2016). To assess the importance of wave-current interactions
38 during a tropical cyclone, we investigated the transport of drifting particles
39 on the Florida shelf during Hurricane Irma, one of the strongest and costliest
40 tropical cyclones on record in the Atlantic Basin (Xian et al., 2018), which
41 made landfall in Florida in September 2017.

42 In this study, we developed an unstructured coupled wave-current model of
43 South Florida to simulate the ocean circulation during hurricane Irma. Both
44 modelled currents and waves were validated against field measurements and
45 were then used to simulate the transport of drifting material in the Florida
46 Keys and the Florida inner shelf during the storm. Model outputs were then
47 compared with uncoupled simulation results in order to assess the impact of
48 wave-induced forces and Stokes drift on the modelled currents and transports.

49 **2. Methods**

50 *2.1. Study area and observational data*

51 Large-scale ocean circulation around South Florida is dominated by the
52 Florida Current (FC), which originates from the Loop Current (LC) where it
53 enters the Florida Straits from the Gulf of Mexico, and, downstream, forms
54 the Gulf Stream. The FC is a major western boundary current characterized
55 by spatial variability and meandering, associated with the presence of cyclonic
56 eddies between the core of the current and the complex reef topography of the
57 Florida Reef Tract (FRT) (Lee et al., 1995; Kourafalou and Kang, 2012). The
58 northern half of these reefs are made of early Holocene reef frameworks and
59 indurated sand ridges while the southern part (the Florida Keys) is composed
60 of a chain of limestone islands, fossilized remnants of ancient coral reefs and
61 sand bars (Hoffmeister and Multer, 1968; Shinn, 1988; Lidz and Shinn, 1991).
62 The variability of the FC extends over a large range of spatial and temporal
63 scales, with periods of 30-70 days in the Lower Keys (Lee et al., 1995) and
64 shorter periods of 2-21 days in the Upper Keys (Lee and Mayer, 1977), and
65 exhibits significant seasonal and interannual cycles (Johns and Schott, 1987;
66 Lee and Williams, 1988; Schott et al., 1988). Circulation on the West Florida
67 Shelf (WFS) on the other hand is forced by local winds and tidal fluctuations
68 (Lee and Smith, 2002; Liu and Weisberg, 2012).

69 The state of the ocean around Florida is monitored by an extensive
70 array of tide gauges, current meters and buoys. In this study, we used sea
71 surface elevation measurements from the National Oceanic and Atmospheric
72 Administrations (NOAA) Tides and Currents dataset. These measurements
73 were taken at four locations: two in the Florida Keys (Key West and Vaca Key);
74 one on the eastern coast of Florida (Virginia Key); and one on the western
75 coast (Naples). For the currents, we used ADCP measurements from the
76 University of South Florida's College of Marine Science's (USF/CMS) Coastal
77 Ocean Monitoring and Prediction System (COMPS) for the WFS (Weisberg
78 et al., 2009). More specifically, we used measurements from moorings C10,

⁷⁹ C12 and C13, respectively located at the 25, 50, and 50 m isobaths of the
⁸⁰ WFS (Liu et al., 2020). Finally, for the waves, we used measurements from
⁸¹ four buoys of the NOAA's National Data Buoy Center (NDBC); two on
⁸² Florida's Eastern shelf and two on the WFS. The locations of all measurement
⁸³ stations are shown on Fig. 1A,C.

⁸⁴ *2.2. Wind and atmospheric pressure during Hurricane Irma*

⁸⁵ Irma made landfall in Florida on 10 September 2017 as a category 3
⁸⁶ hurricane, first at Cudjoe Key (Florida Keys) and later on Marco Island,
⁸⁷ south to Naples (see hurricane track in Fig. 1). It then weakened to a
⁸⁸ category 2 hurricane as it moved further inland (Pinelli et al., 2018). The
⁸⁹ storm damaged up to 75% of the buildings at his landfall point in the Florida
⁹⁰ Keys, making it one of the strongest and costliest hurricanes on record in the
⁹¹ Atlantic basin (Xian et al., 2018; Zhang et al., 2019). The strongest reported
⁹² wind speed was 50 m/s on Marco Island while the highest recorded storm
⁹³ surge was 2.3 m, although larger wind speed likely occurred in the Florida
⁹⁴ Keys (Pinelli et al., 2018) In order to reproduce the wind profile of Irma in
⁹⁵ our model, we used high-resolution H*Wind wind fields (Powell et al., 1998).
⁹⁶ As these data represent 1-min averaged wind speeds, we multiplied them by
⁹⁷ a factor 0.93 to obtain 10-min averaged wind speeds (Harper et al., 2010),
⁹⁸ which are more consistent with the time step of our model. Furthermore,
⁹⁹ H*Wind wind profiles did not cover the whole model extent during the
¹⁰⁰ passage of the hurricane and were thus blended within coarser wind field
¹⁰¹ extracted from ECMWF ERA-5 datasets (Fig. 2A). Pressure fields of Irma
¹⁰² were also constructed using ERA-5 data. However, the coarse resolution of
¹⁰³ the dataset smooth out the depression at the center of the hurricane, leading
¹⁰⁴ to an underestimation of the pressure gradient in our model (Fig. 2B). To
¹⁰⁵ better capture the central depression of Irma, we built a hybrid pressure field
¹⁰⁶ using the position and the minimal pressure of the core of the hurricane based
¹⁰⁷ on its track as recorded in the HURDAT 2 database (Landsea and Franklin,
¹⁰⁸ 2013). Based on this information, the hybrid pressure field was constructed

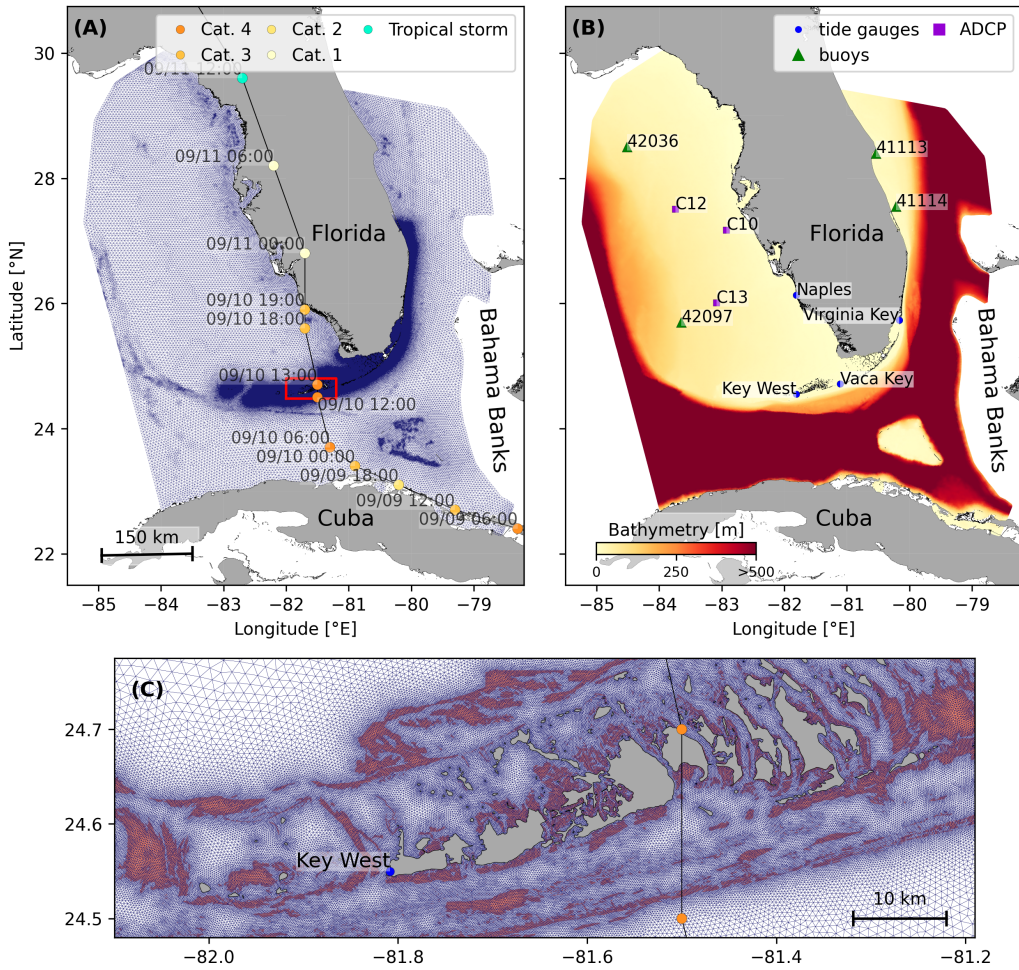


Fig. 1: **A:** Mesh of the computational domain with the trajectory of Irma, category of the hurricane is given by the Saffir-Simpson color scale. **B:** Bathymetry of the domain with the location of stations used for the validation of the model outputs. **C:** Close up view of the Lower Keys area, where the mesh resolution reaches 100m near reefs (shown in dark orange) and islands (highlighted in dark grey)

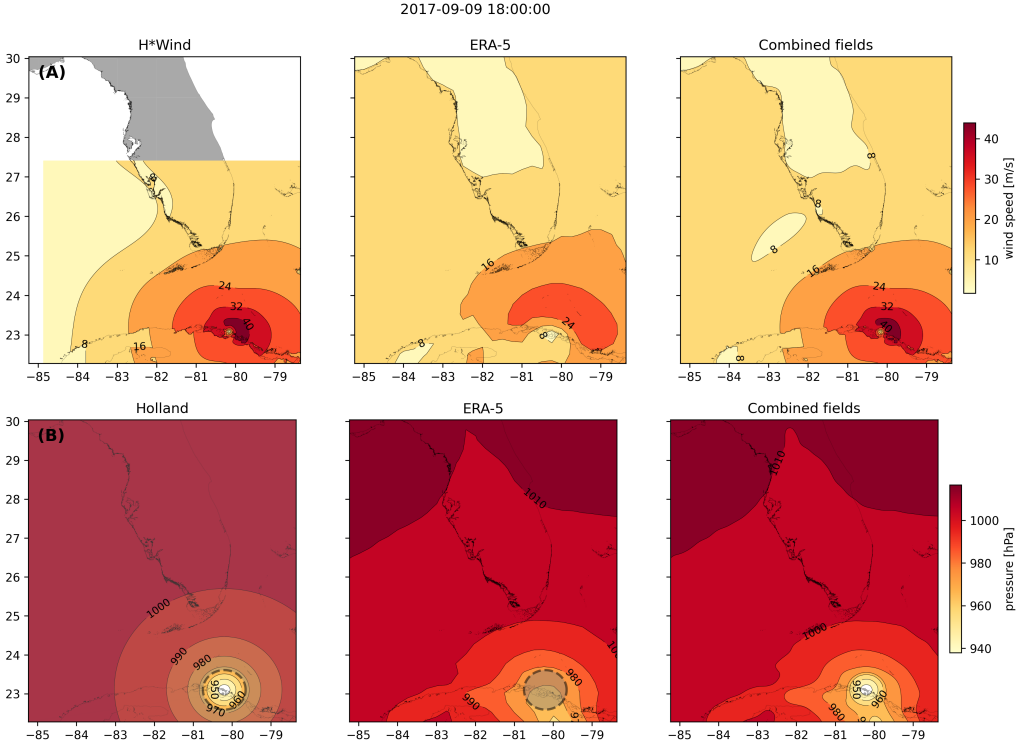


Fig. 2: Snapshot of the hybrid wind and pressure profiles constructed to capture the passage of Hurricane Irma at 1800 UTC 9 September 2017. Wind profiles are obtained by combining high resolution H*Wind with coarse ERA-5 wind fields. Pressure fields are built by combining RA-5 pressure field with an idealized Holland pressure profile based on the track of Irma in the HURDAT 2 database. Holland field was only used within the radius of maximum wind speed (discontinuous grey line) of the hurricane to capture its central depression.

109 by combining an idealized Holland pressure profile (Lin and Chavas, 2012)
 110 within the radius of maximum wind speed of Irma (Knaff et al., 2018) with
 111 ERA-5 pressure field. The transition between from the Holland profile to
 112 ERA-5 data outside the radius of maximum wind speed data was performed
 113 using a smooth step function (Fig. 2).

114 *2.3. Hydrodynamic model*

115 Ocean currents generated during hurricane Irma around South Florida
 116 were modelled using the 2D barotropic version of the unstructured-mesh

117 coastal ocean model SLIM¹. The model mesh covers an area similar to the
 118 model extent of Dobbelaere et al. (2020b), that includes the FRT but also the
 119 Florida Straits and part of the Gulf of Mexico (Figure 1). However, this area
 120 has been slightly extended northeastward and westward in order to include
 121 the NOAA-NDBC buoys. Furthermore, to withstand potential cell drying
 122 during the hurricane, we solved the conservative shallow water equations with
 123 wetting-drying:

$$\begin{aligned}
 \frac{\partial H}{\partial t} + \nabla \cdot (\mathbf{U}) &= 0 , \\
 \frac{\partial \mathbf{U}}{\partial t} + \nabla \cdot \left(\frac{\mathbf{U}\mathbf{U}}{H} \right) &= -f\mathbf{e}_z \times \mathbf{U} + \alpha g H \nabla(H - h) - \frac{1}{\rho} \nabla p_{\text{atm}} + \frac{1}{\rho} \boldsymbol{\tau}_s \quad (1) \\
 &\quad + \nabla \cdot (\nu \nabla \mathbf{U}) - \frac{C_b}{H^2} |\mathbf{U}| \mathbf{U} + \gamma (\mathbf{U}_{\text{ref}} - \mathbf{U}) ,
 \end{aligned}$$

124 where H is the water column height and \mathbf{U} is the depth-averaged transport;
 125 f is the Coriolis coefficient; g is the gravitational acceleration; h is the
 126 bathymetry; α is a coefficient stating whether the mesh element is wet ($\alpha = 1$)
 127 or dry ($\alpha = 0$) [*add more detail about impact of wetting-drying ?*]; ν is the
 128 viscosity; C_b is the bulk bottom drag coefficient; ∇p_{atm} is the atmospheric
 129 pressure gradient; $\boldsymbol{\tau}_s$ is the surface stress, usually due to wind; and γ is a
 130 relaxation coefficient towards a reference transport \mathbf{U}_{ref} . As in Frys et al.
 131 (2020) and Dobbelaere et al. (2020b), SLIM currents were gradually relaxed
 132 towards the operational Navy HYCOM product (GOMl0.04², Chassignet et al.
 133 (2007)) in regions where the water depth exceeds 50m.

134 At very high wind speeds, the white cap is blown off the crest of the waves
 135 (also known as spumes), which has been hypothesized to generate a layer
 136 of droplets that acts as a slip layer for the winds at the ocean-atmosphere
 137 interface (Holthuijsen et al., 2012). This causes a saturation of the wind drag
 138 coefficient for strong winds (Donelan et al., 2004; Curcic and Haus, 2020;

¹<https://www.slim-ocean.be>

²<https://www.hycom.org/data/goml0pt04>

¹³⁹ Powell et al., 2003). To account for the impact of this saturation on the surface
¹⁴⁰ wind stress in our model, we implemented the wind drag parameterization of
¹⁴¹ Moon et al. (2007). In this parameterization, the drag coefficient C_d depends
¹⁴² on the wind speed at 10-m height U_{10} according to:

$$C_d = \kappa^2 \log \left(\frac{10}{z_0} \right)^{-2} \quad (2)$$

¹⁴³ where κ is the von Karman constant. The roughness length z_0 in Eq. (2) is
¹⁴⁴ expressed as:

$$z_0 = \begin{cases} \frac{0.0185}{g} U_*^2 & \text{if } U_{10} \leq 12.5 \text{ m/s ,} \\ [0.085(-0.56U_*^2 + 20.255U_* + 2.458) - 0.58] \times 10^{-3} & \text{if } U_{10} > 12.5 \text{ m/s ,} \end{cases} \quad (3)$$

¹⁴⁵ with U_* the friction velocity. The relation between U_{10} and U_* is given by:

$$U_{10} = -0.56U_*^2 + 20.255U_* + 2.458 . \quad (4)$$

¹⁴⁶ The mesh resolution depends on the distance to coastlines and reefs
¹⁴⁷ following the approach of Dobbelaere et al. (2020b). The mesh is then further
¹⁴⁸ refined according to bathymetry value and gradient, as suggested in the
¹⁴⁹ SWAN user-guide³. Such an approach improves the model efficiency as the
¹⁵⁰ mesh resolution is only increased where required by the currents and waves
¹⁵¹ dynamics. The mesh was generated with the seamsh⁴ Python library, which is
¹⁵² based on the open-source mesh generator GMSH (Geuzaine and Remacle,
¹⁵³ 2009). It is composed of approximately 7.7×10^5 elements. The coarsest
¹⁵⁴ elements, far away from the FRT, has a characteristic length of about 5 km
¹⁵⁵ whereas the finest elements have a characteristic length of about 100 m near

³<http://swanmodel.sourceforge.net/unswan/unswan.htm>

⁴<https://pypi.org/project/seamsh/>

156 coastlines and reefs (Fig 1).

157 *2.4. Wave model*

158 Waves were modelled using the parallel unstructured-mesh version of the
159 Simulating WAves Nearshore (SWAN) model (Booij et al., 1999), one of the
160 most commonly used wave models in coastal areas and inland waters. This
161 model solves the action balance equation (Mei, 1989):

$$\frac{\partial N}{\partial t} + \nabla_{\mathbf{x}} \cdot [(\mathbf{c}_g + \mathbf{u})N] + \frac{\partial}{\partial \theta}[c_\theta N] + \frac{\partial}{\partial \sigma}[c_\sigma N] = \frac{S_{in} + S_{ds} + S_{nl}}{\sigma}, \quad (5)$$

162 where $N = E/\sigma$ is the wave action density and E is the wave energy spectrum;
163 θ is the wave propagation direction; σ is the intrinsic wave frequency; \mathbf{c}_g is
164 the wave group velocity, $\mathbf{u} = \mathbf{U}/H$ is SLIM depth-averaged current velocity;
165 c_θ and c_σ are the propagation velocities in spectral space due to refraction
166 and shifting in frequency due to variations in depth and currents; and S_{in} ,
167 S_{ds} , and S_{nl} respectively represent wave growth by wind, wave decay and
168 nonlinear transfers of wave energy through interactions between triplets
169 and quadruplets. Spectra were discretized with 48 direction bins and 50
170 frequency bins logarithmically distributed from 0.03 to 2 Hz. Exponential
171 wind growth was parameterized using the formulation of Janssen (1991),
172 while dissipations by whitecapping and bottom dissipations followed the
173 formulations of Komen et al. (1984) and Madsen et al. (1989), respectively.
174 Coefficients for exponential wind growth and whitecapping parameterizations
175 were based on the results of Siadatmousavi et al. (2011), and significantly
176 differ from SWAN's default settings. By default, SWAN implements the
177 wind input formulation of Komen et al. (1984) and the steepness-dependent
178 coefficient governing dissipation by whitecapping is a linear function of the
179 wave number. In this study, this steepness-dependent coefficient is a quadratic
180 function of the wave number, as it showed better predictions of the significant
181 wave height in the study of Siadatmousavi et al. (2011). The choice of these
182 formulations was motivated by the appearance of numerical instabilities in

183 the region of the Gulf Stream when using SWAN's default parameter values.
 184 Finally, wave boundary conditions were derived from WAVEWATCH III
 185 (Tolman et al., 2009) spectral outputs at NDBC buoy locations. We selected
 186 these datasets as the large number of NDBC buoys around our region of
 187 interest allowed for a fine representation of the wave spectra on the boundary
 188 of the domain.

189 Surface waves induce a net drift in the direction of the wave propagation,
 190 known as the Stokes drift (Van Den Bremer and Breivik, 2018; Stokes,
 191 1880). This net drift has a significant impact on sediment transport in
 192 nearshore regions (Hoefel and Elgar, 2003), on the formation of Langmuir
 193 cells (Langmuir, 1938; Craik and Leibovich, 1976) as well as on the transport
 194 of heat, salt or pollutants such as oil or micro-plastic in the upper ocean layer
 195 (McWilliams and Sullivan, 2000; Röhrs et al., 2012; Drivdal et al., 2014). To
 196 correctly model the Stokes drift profile in mixed wind-driven sea and swell
 197 conditions, the full two-dimensional wave spectrum must be represented by
 198 a spectral wave model within a wave-current coupling (Van Den Bremer and
 199 Breivik, 2018). In this study, the depth-averaged Stokes drift was therefore
 200 computed by SWAN using the following formula:

$$\mathbf{u}_s = \int_0^{2\pi} \int_0^{+\infty} \frac{\sigma^3}{h \tanh(2kh)} E(\sigma, \theta) (\cos \theta, \sin \theta) d\sigma d\theta , \quad (6)$$

201 where k is the norm of the wave vector; h is the water depth; and $E(\sigma, \theta)$ is
 202 the wave energy density.

203 2.5. Coupled model

204 SLIM and SWAN are coupled so that they run on the same computational
 205 core and the same unstructured mesh. SLIM is run first and passes computed
 206 wind velocities (\mathbf{U}_{10}), water levels ($\eta = H - h$) and depth-averaged currents
 207 ($\mathbf{u} = \mathbf{U}/H$) to SWAN, as well as a roughness length (z_0) for the bottom
 208 dissipation formulation of Madsen et al. (1989). This roughness length is
 209 computed from SLIM's bulk drag coefficient C_b following the approach of

210 Dietrich et al. (2011) so that both models have consistent bottom dissipation
211 parameterizations. SWAN then uses these quantities to compute the wave
212 radiation stress gradient, that is then passed to SLIM as the force exerted
213 by waves on currents τ_{wave} (Fig. 3). SLIM then uses this quantity to
214 update the the value of the surface stress τ_s in Eq. (1), that now becomes
215 the sum of wind and wave-induced stresses $\tau_s = \tau_{\text{wind}} + \tau_{\text{wave}}$. Here, the
216 momentum flux from the atmosphere to the ocean is taken as the commonly-
217 used full wind tress τ_{wind} . Doing so, we neglect the momentum advected
218 away from the storm by the waves, leading to a 10-15% overestimation of
219 the momentum flux in hurricane winds Curcic (2015). Moreover, we followed
220 the approach of Dietrich et al. (2012) by characterizing the wave-induced
221 stresses using the radiation-stress representation instead of the vortex-force
222 representation (McWILLIAMS et al., 2004). Although the later provides a
223 clearer and meaningful decomposition of the wave-effect, we implemented the
224 first representation for the sake of simplicity as it allows us to provide the
225 whole wave contribution as an additional surface stress to SLIM (Lane et al.,
226 2007).

227 SLIM’s governing equations are integrated using an implicit time inte-
228 gration scheme while SWAN is unconditionally stable (Dietrich et al., 2012),
229 allowing both models to be run with relatively large time steps. In this study,
230 the stationary version of SWAN was used, *i.e.* the time derivative of Eq. 5
231 was set to zero. This resulted in reduced scaling and convergence rates than
232 with the nonstationary version of SWAN but increased the stability of the
233 model. The wave spectra at each node of the mesh was saved at the end of
234 each iteration to serve as initial conditions for the next one. Both models
235 were run sequentially using a time step of 600s, so that each computational
236 core was alternating running either SLIM or SWAN. As in the coupling
237 between SWAN and ADCIRC (Dietrich et al., 2012), both models utilize the
238 same local sub-mesh, allowing for a one-to-one correspondence between the
239 geographic locations of the mesh vertices. No interpolation is therefore needed

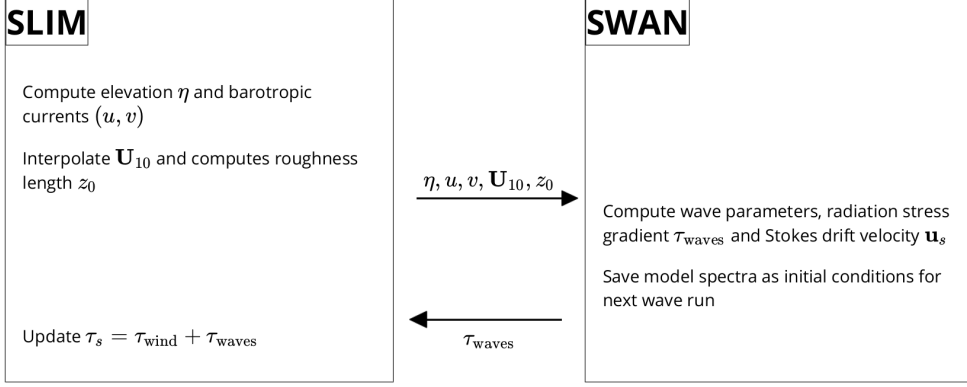


Fig. 3: Schematic illustration of the coupled SLIM+SWAN model.

when passing the discretised variables from one model to the other, which allows an efficient inter-model communication. However, as SLIM applies discontinuous Galerkin finite element methods, an additional conversion step to a continuous framework was required to transmit SLIM nodal quantities to SWAN.

3. Results

We first validated the reconstructed atmospheric fields of hurricane Irma as well the modelled currents and waves of our coupled model against fields measurements. A summary of the error statistics is given in Table 1. We then use the validated model to simulate the transport of passive drifters in the Lower Keys during the passage of Hurricane Irma. These drifters were advected by two sets of currents: (i) the currents from an uncoupled SLIM simulation of Irma (SLIM) and (ii) the currents modelled by the coupled SLIM+SWAN model (SLIM+SWAN). Furthermore, the depth-averaged Stokes drift was computed using our coupled model (Stokes_C) and an uncoupled SWAN simulation of the hurricane (Stokes_U). We then simulated the trajectories of passive tracers during the passage of the Irma in the Lower Keys using different combinations of these fields. These trajectories were

258 finally compared to evaluate the impact of the wave-current interactions and
259 the Stokes drift on the transport processes during a major hurricane.

260 *3.1. Model validation*

261 H*Wind winds and hybrid pressure field agree well with station mea-
262 surements at Vaca Key station (Fig. 4). The hybrid pressure field shows
263 better agreement with observations than ERA-5 pressure as it successfully
264 reproduces the storm depression. ERA-5 fields, on the other hand, fail to
265 resolve the low pressure at the core of the hurricane due to their coarser
266 grid, leading to an overestimation of 8 mbar of the storm depression. Both
267 H*Wind and ERA-5 agree well with observed wind speeds although both
268 data sets tend to slightly overestimate the width and intensity of the wind
269 peak. However, H*wind profiles show a better match with the timing of the
270 observed peak, as ERA-5 winds tend to anticipate it. H*wind also exhibits a
271 slightly narrower peak in wind speed, which better agrees with observations.

272 Hydrodynamic outputs of the coupled wave-current model agree well
273 with tide gauge (Fig. 5) and ADCP measurements (Fig. 6). Despite a
274 slight overestimation of the amplitude of sea surface elevation (1) in fair
275 weather conditions, the timing and amplitude of the storm surges are well
276 reproduced by the coupled model. The largest model error during the surge
277 is an overestimation of 18 cm of the elevation peak at Virginia Key. The
278 fit is especially good at Naples, where both the large positive and negative
279 surges are captured by the coupled model with an error of less than 5 cm.
280 This result is of interest as negative surges, although less studied, affect
281 water exchanges between the estuaries and the coastal ocean and disturb the
282 benthic ecosystems (Liu et al., 2020). Modelled 2D currents were validated
283 against depth-averaged ADCP measurements at mooring station C10, C12
284 and C13 (Fig. 6). As in Liu et al. (2020), we performed the vector correlation
285 analysis of Kundu (1976) to compare modelled and observed current velocity
286 vectors. Correlation coefficients (ρ) between simulated and observed depth-
287 averaged currents were 0.84, 0.74 and 0.73 at the C10, C12 and C13 locations,

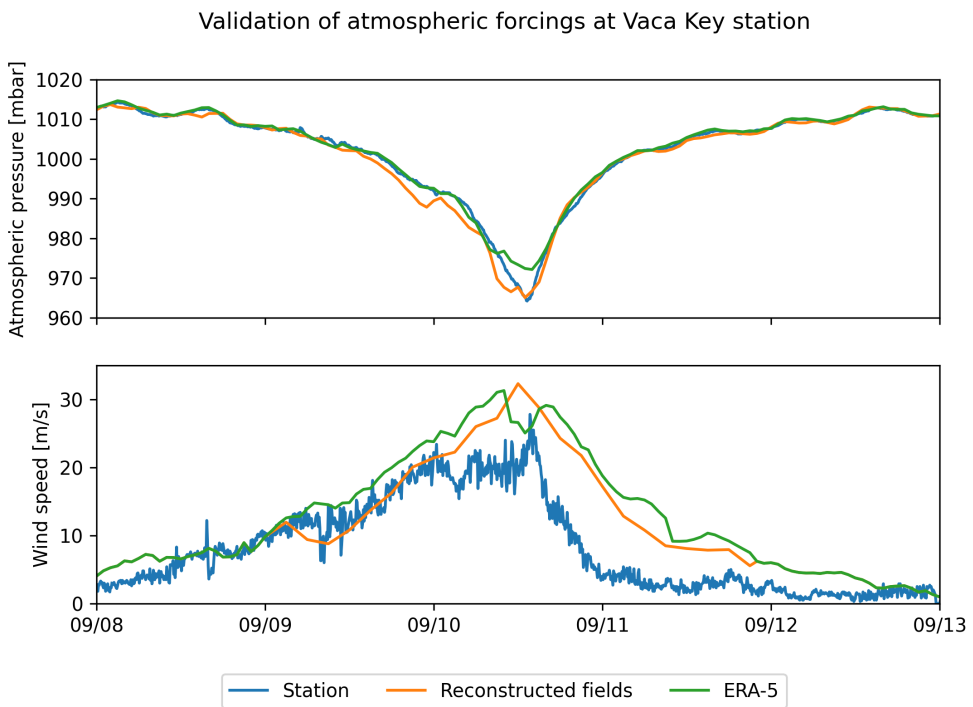


Fig. 4: Comparison of reconstructed wind atmospheric pressure with field measurements and coarser ECMWF ERA-5 profiles at Vaca Key station. The generated hybrid atmospheric forcings better capture the observed storm depression while H*wind winds better match the measured peak in wind speed.

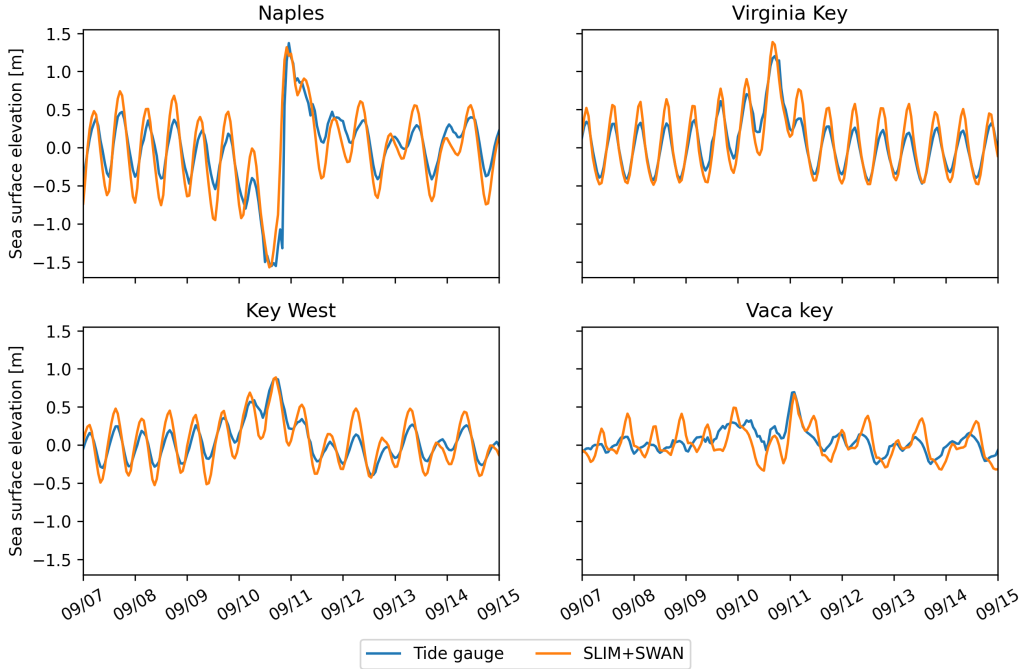


Fig. 5: Comparison of modelled sea surface elevation with all 4 tide gauge measurements (see Fig. 1B for their location). Timing and amplitudes of the storm surges are well reproduced by the model

respectively. Average veering angles were computed as well and were below 12° , as in (Liu et al., 2020). Furthermore, Table 1 indicates that our model tends to produce larger prediction errors on the northward component of the depth-averaged currents than the eastward one. As expected from a depth-averaged model, the best fit with observations is obtained at the shallowest mooring C10, located on the 25m isobath, with an average veering angle of 6° and smaller error statistics (Table 1).

The simulated significant wave height agrees well with observations on the WFS, where errors on the peak value do not exceed 5% (Fig. 7). On the eastern shelf of Florida, errors are slightly larger and reach 20%. Although the model outputs agree well with observations, a lag in significant wave height is observed for all 4 buoys. Moreover, the peak in significant wave

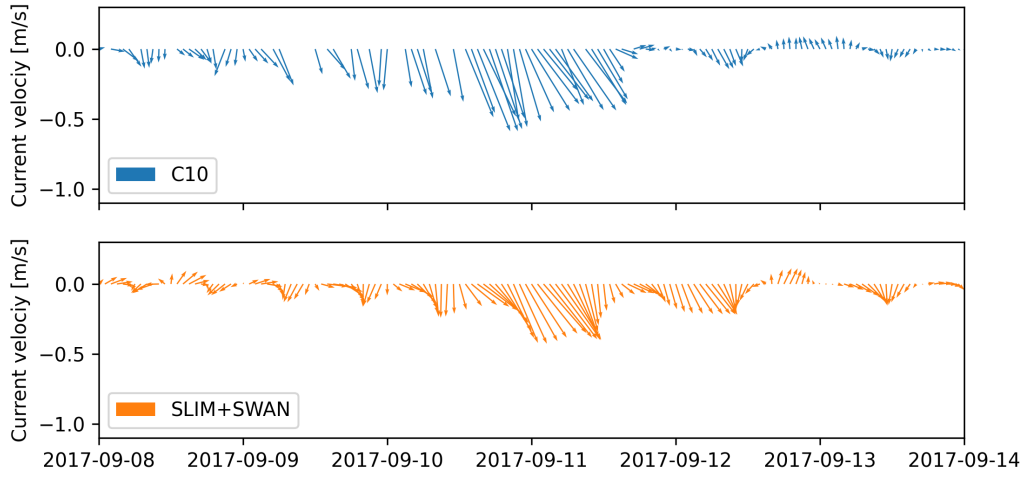


Fig. 6: Comparison of modelled current velocity with observed velocity at mooring C10 (see Fig. 1B for its location). Modelled current velocities agree well with observations, with a correlation coefficient of 0.83 and an average veering angle of 6° .

height tends to be underestimated at buoys 41113 and 41114, located on the East Florida Shelf. Other wave parameters were better reproduced by the model on the WFS as well (see buoy 42036 in Fig. 7 and Table 1). This good fit on the WFS is not surprising as the parameters used for wind energy input and whitecapping dissipation were based on the calibration performed by Siadatmousavi et al. (2011) on the Northern Gulf of Mexico. Wind-induced wave growth might therefore be underestimated on the eastern shelf. Consequently, incident wave do not receive enough energy to grow after breaking on the bank boundary, leading to an underestimation of the significant wave height at the location of the buoys. Nonetheless, as this study focused on the wave produced by Irma, which made landfall on the western coasts of Florida, the use of parameterizations calibrated for the Gulf of Mexico seems reasonable.

3.2. Impact of waves on currents and transport

We evaluated the impact of wave-current interactions on modelled currents during the passage of Irma in the Lower Keys, between Sept. 7 and 13, 2017.

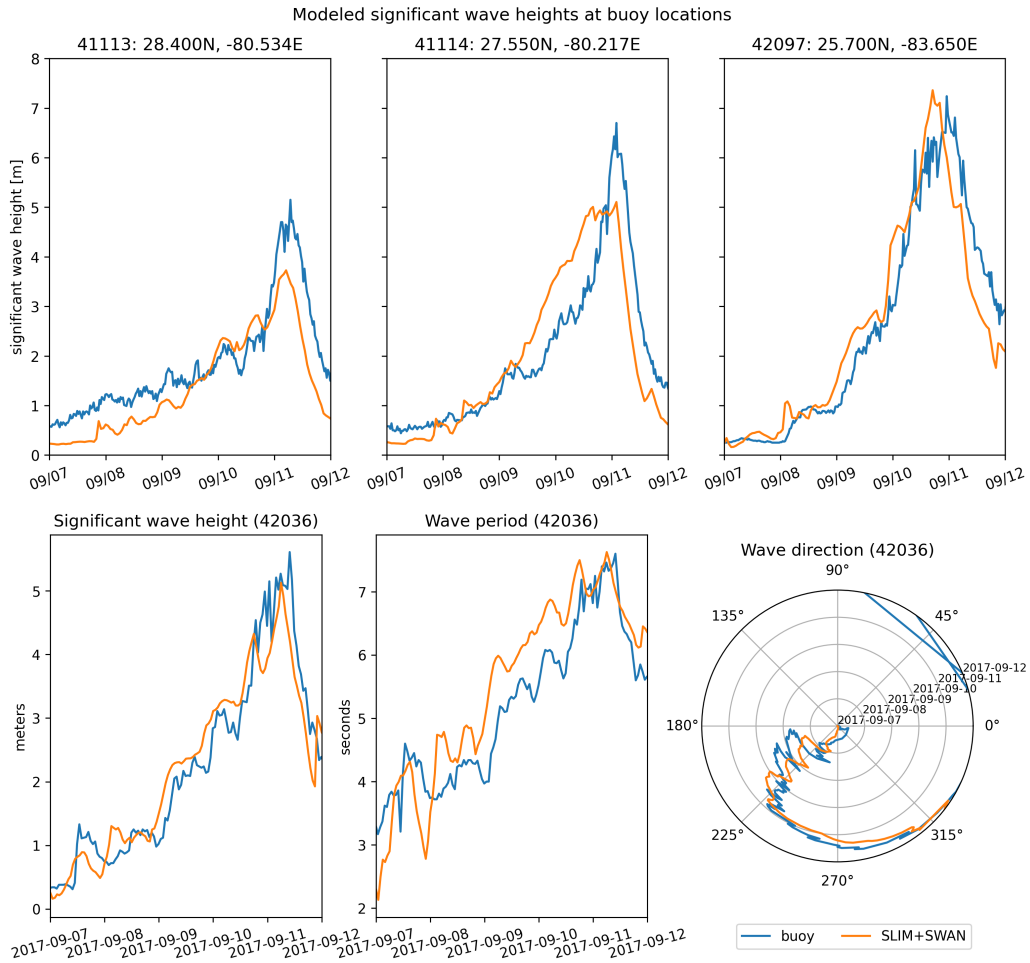


Fig. 7: Comparison of modelled wave parameters with observation at the 4 buoys location (locations shown in Fig. 1B). Modelled significant wave height agrees well with field measurement. As model parameters were calibrated for the Northern Gulf of Mexico, observations are better reproduced at buoys located on the WFS, as illustrated for buoy 42036

Station	Variable	Bias	MAE	RMSE
Vaca Key	sse (m)	n/a	0.12	0.16
	U_{10} (m/s)	1.51	1.85	2.61
	p_{atm} (hPa)	-0.21	0.59	1.03
Key West	sse (m)	n/a	0.11	0.13
Virginia Key	sse (m)	n/a	0.10	0.13
Naples	sse (m)	n/a	0.18	0.23
C10	u (m/s)	-0.006	0.04	0.05
	v (m/s)	0.02	0.06	0.08
C12	u (m/s)	-0.01	0.06	0.07
	v (m/s)	0.06	0.09	0.11
C13	u (m/s)	0.004	0.06	0.08
	v (m/s)	0.04	0.06	0.08
41113	H_s (m)	-0.35	0.40	0.51
	T_m (s)	-2.18	2.47	3.13
41114	H_s (m)	-0.21	0.53	0.68
	T_m (s)	-1.69	2.53	3.15
42036	H_s (m)	-0.03	0.26	0.36
	T_m (s)	0.04	0.65	0.77
42097	H_s (m)	-0.15	0.40	0.57
	T_m (s)	0.02	0.62	0.74

Table 1: Error statistics comparing SLIM+SWAN simulated quantities with the measured sea surface elevation (sse), eastward and northward depth-average current velocities (u,v), significant wave height (H_s), and zero-crossing mean wave period (T_m). Model bias, mean absolute error (MAE), and root mean squared error (RMSE) are listed by variable (unit) and value.

316 First, we computed the maximum difference between currents modelled by
317 SLIM and SLIM+SWAN during this period (Fig. 8A). The largest differences
318 in current speed were observed over the reefs, on the shelf break and around
319 islands. They can locally reach 1 m/s, with the coupled model SLIM+SWAN
320 yielding the largest amplitudes. The regions where the differences are the
321 largest experience the largest wave-induced stress τ_{wave} (Fig. 8B), as wave
322 breaking and wave slowing down over rough seabed induce variations of the
323 wave radiation stress (Longuet-Higgins and Stewart, 1964). Wave-induced
324 differences in current speed were amplified by the action of the wind stress
325 τ_{wind} (Fig. 8C). Wind speeds were larger in the front right quadrant of the
326 hurricane (Zedler et al., 2009), yielding larger differences on the right-hand
327 side of the storm trajectory. This is especially clear in the area between
328 the Florida Keys and the Everglades, where relatively small values of τ_{wave}
329 nonetheless produce current speed differences of up to 0.5 m/s because of the
330 wind stress.

331 To quantify the impact of these differences in the velocity fields, we
332 compared the trajectories of passive particles advected by the uncoupled
333 SLIM and coupled SLIM+SWAN currents during the passage of Irma in the
334 Lower Keys (Fig. 9). Particles were released on the inner and outer shelves
335 at the points highlighted in red and blue dots in Fig. 9A on 7 September
336 and then tracked until 15 September. These areas were constructed using
337 backtracking methods (Dobbelaeere et al., 2020a) to ensure that the release
338 particles would intersect the path of Irma during its passage in the Florida
339 Keys. We first defined two 25km² circular regions on the trajectory of the
340 hurricane (see red and blue circles in Fig. 9A). Particles within these two
341 regions were then tracked backward in time using uncoupled SLIM currents
342 from the exact time of the passage of the hurricane until the 7th of September.
343 Their positions at the end of the backward simulation (see red and blue
344 particle clouds in Fig. 9) corresponds to the initial condition of the forward
345 transport simulations described below.

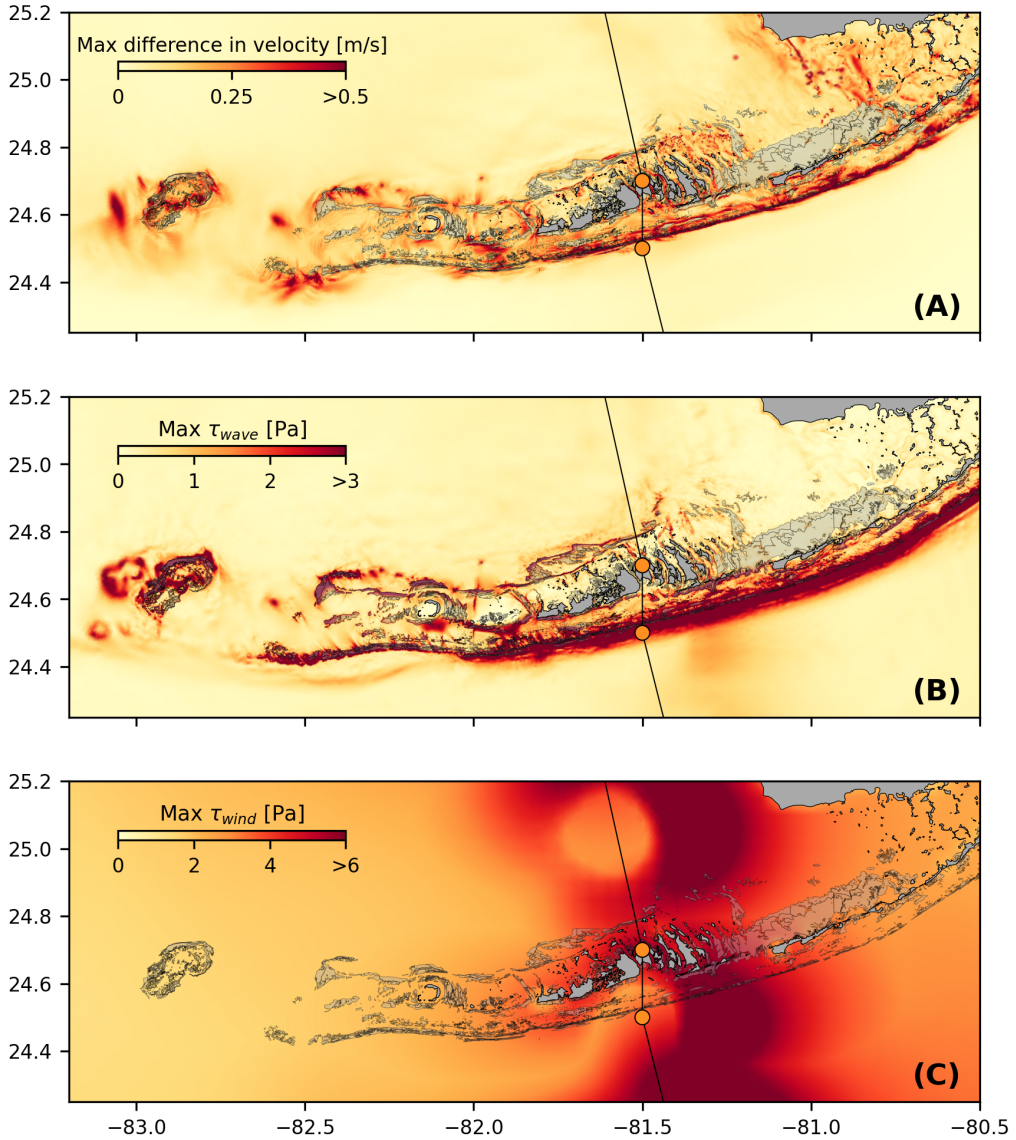


Fig. 8: Maximum difference between SLIM and SLIM+SWAN currents (A) during the passage of Irma in the Lower Florida Keys, along with the maximum wave radiation stress gradient τ_{wave} (B) and wind stress τ_{wind} (C) generated by the hurricane. Wave-induced stress yields difference larger than 0.5 m/s in current velocities. These wave-induced differences in currents were amplified by the action of the asymmetric wind profile of Irma, with larger differences occurring on the right of the storm trajectory

346 We compared the trajectories of particles originating from these regions
347 and advected forward in time by different sets of currents: (i) uncoupled SLIM
348 currents alone; (ii) coupled SLIM+SWAN currents; (iii) SLIM currents with
349 the addition of the depth-averaged Stokes drift computed by the coupled wave
350 model (Stokes_C); (iv) SLIM+SWAN currents with Stokes_C; and (v) SLIM
351 currents with the depth-averaged Stokes drift computed by the uncoupled
352 wave model (Stokes_U). Particles trajectories are compared by computing
353 the distances between the centers of mass of the particle clouds through
354 time. Here are our main observations (*this needs to be improved, feedback is*
355 *welcome!*) :

- 356 • The impact of wave-current interactions is the most important during the
357 passage of the hurricane but negligible during the rest of the simulated
358 period. This is clear when comparing the clouds of particles advected
359 by SLIM and SLIM+SWAN on the outer shelf [plot clouds of particles
360 to make it clearer]. The distance between the centers of mass reaches 5
361 km during the passage of Irma but is negligible during the rest of the
362 simulated period.
- 363 • The impact of the Stokes drift is larger than the impact of the wave-
364 current interactions on the inner shelf. The difference between the
365 centers of mass does not exceed \sim 1 km for SLIM vs SLIM+SWAN but
366 reaches about 5 km for SLIM vs SLIM+Stokes_C and SLIM+SWAN+Stokes_C.
367 On the outer shelf, the currents are more intense and the impact the
368 wave-current coupling during the passage of the hurricane is sufficient
369 to generate a difference between the two clouds of particles that keeps
370 on increasing after the passage of the hurricane. The impact of the
371 Stokes drift remains however larger than the impact of the wave-current
372 coupling. This difference between the inner and outer shelf can be
373 explained by the sheltering of the inner shelf due to reefs and islands
374 as well as wave breaking on the shelf break. The inner shelf hence
375 experiences weaker waves and weaker currents, and hence also weaker

376 and more localised transport.

- 377
- 378 • On the inner shelf, the distance between the centers of mass of the
379 particle clouds stabilizes after the passage of the hurricane while this
380 distance keeps increasing during a couple of days after the passage of
381 the hurricane on the outer shelf under the action of the Stokes drift.
382 This shows the strong impact of wave-induced transport in the open
ocean.
 - 383 • Impact of Stokes drift and wave-current interactions weaker on the inner
384 shelf. Max. distance of about 5 km between the centers of mass of the
385 clouds of particles compared to 30km on the outer shelves
 - 386 • The fact that SLIM+Stokes_C vs. SLIM+Stokes_U keeps increasing on
387 the outer shelf after the passage of the hurricane shows the impact of
388 the strong current velocities of the FC on the modelled Stokes drift
 - 389 • Nonetheless, the differences between the coupled and uncoupled Stokes
390 drifts remains relatively small with a maximum value of 2 km between
391 the centers of mass of the simulated particle clouds. Furthermore, as
392 SLIM vs SLIM+SWAN+Stokes and SLIM vs. SLIM+Stokes_C show
393 similar values on the inner shelf, this suggests that the combination
394 of currents and Stokes drifts produces sufficiently accurate results on
395 sheltered shallow areas such as the WFS. However, neglecting the wave-
396 current interactions leads to differences of up to 5 km in modelled
397 particle trajectories on the outer shelf.
 - 398 • Matthieu: Pour la partie discussion, je pense que tu peux essayer de
399 mettre en avant un des avantages du modle, qui est la haute rsolution
400 entre les les des Keys (en plus du couplage avec les vagues). Je pense
401 que a peut faire partie de "impact of waves on coral connectivity" que
402 tu mentionnes dans ta partie 4.

403 [Milan: Two first points could be well summarized in table]

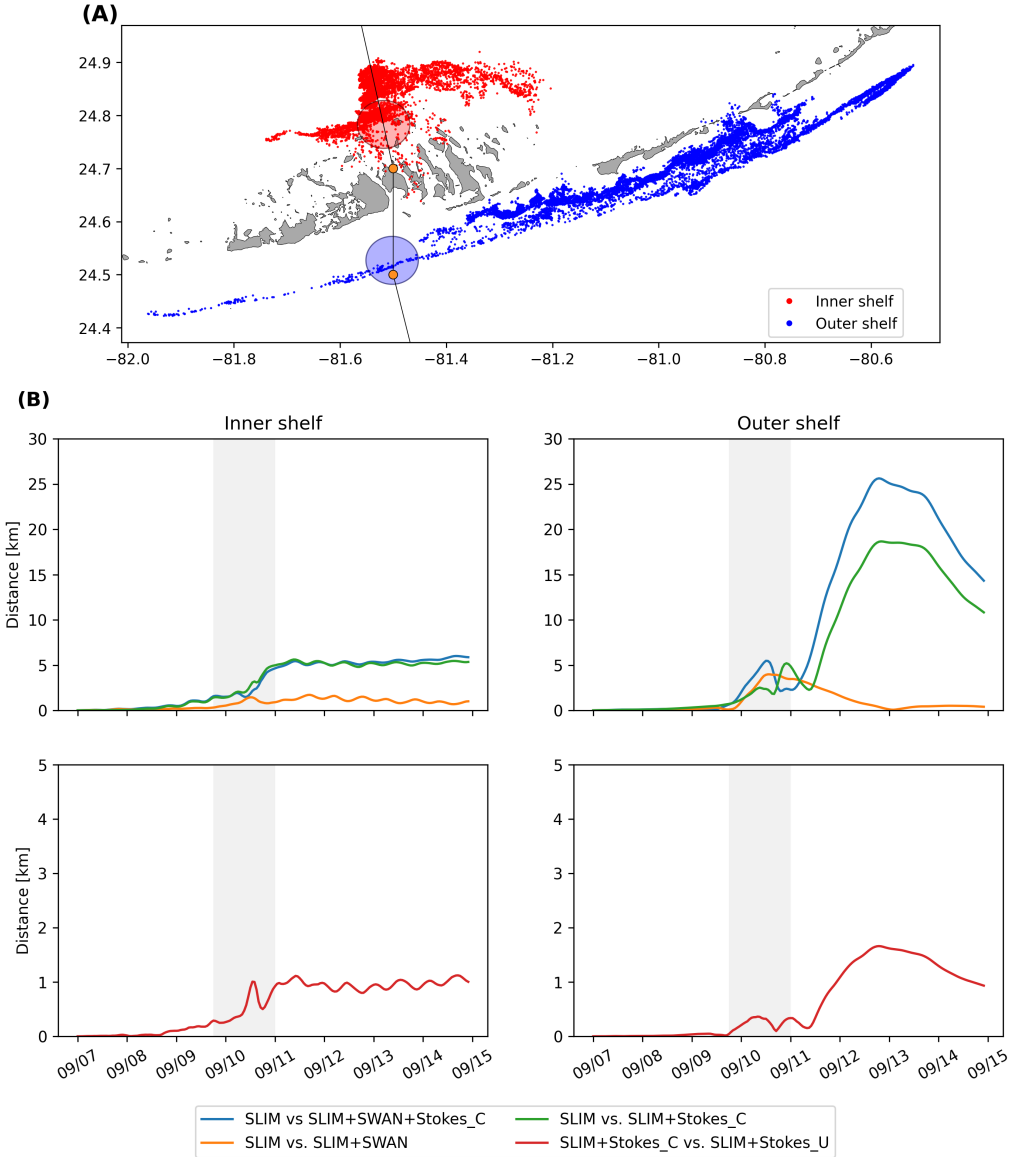


Fig. 9: **A:** Release regions of the passive particles on the inner and outer shelves (red and blue clouds) obtained by backtracking particles released in the red and blue circular areas during the passage of Irma. **B:** Difference between the centers of mass of the particle clouds released from the regions highlighted in **A** and advected by different combinations of coupled and uncoupled velocity fields. **Matthieu: prsenter plus d'informations sur la Figure 8, notamment les nuages de points issus des deux simulations (SLIM et SLIM+SWAN+Stokes_C), ainsi que les centres de masses correspondants. Ca devrait permettre de soutenir la partie rsultats.**

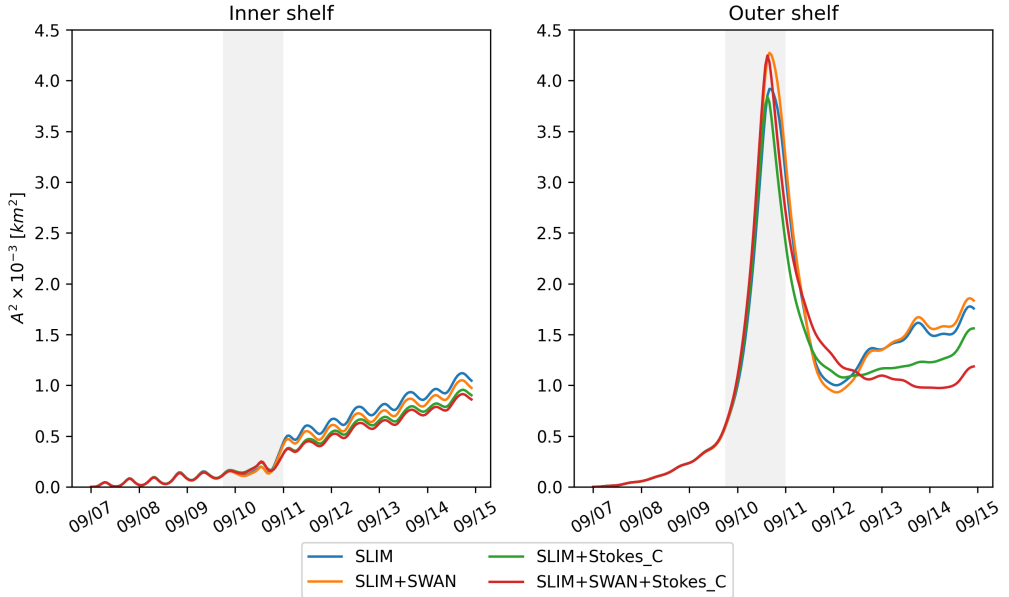


Fig. 10: Dispersion of particles with different velocity fields → not sure to know what to say about that...

404 4. Discussion

405 Impact of waves on coral connectivity

406 Ability of wave model to correctly capture gradient in significant wave
407 height due to current-waves interactions under tropical cyclones depends on:

- 408 • Broad perspective ⇒ not limited to FL
- 409 • Mention search and rescue
- 410 • However, ignoring waves in storm conditions could result in significant
411 inaccuracies in modelled trajectories, as illustrated in the case of release
412 region 2 in Fig. 9
- 413 • Spatial (10km → 5km) and spectral (36 dir. → 48 dir.) resolution
414 (Hegermiller et al., 2019)
- 415 • Directional spreading of incident waves (Villas Bôas et al., 2020)

416 **5. Conclusion**

417 **Acknowledgments**

418 Computational resources were provided by the Consortium des Équipements
419 de Calcul Intensif (CÉCI), funded by the F.R.S.-FNRS under Grant No.
420 2.5020.11. Thomas Dobbelaere is a PhD student supported by the Fund for
421 Research training in Industry and Agriculture (FRIA/FNRS).

422 **References**

- 423 Bever, A.J., MacWilliams, M.L., 2013. Simulating sediment transport pro-
424 cesses in San Pablo Bay using coupled hydrodynamic, wave, and sediment
425 transport models. *Marine Geology* 345, 235–253.
- 426 Booij, N., Ris, R.C., Holthuijsen, L.H., 1999. A third-generation wave
427 model for coastal regions: 1. Model description and validation. *Journal of*
428 *geophysical research: Oceans* 104, 7649–7666.
- 429 Chassignet, E.P., Hurlburt, H.E., Smedstad, O.M., Halliwell, G.R., Hogan,
430 P.J., Wallcraft, A.J., Baraille, R., Bleck, R., 2007. The HYCOM (hybrid
431 coordinate ocean model) data assimilative system. *Journal of Marine*
432 *Systems* 65, 60–83.
- 433 Chen, C., Huang, H., Beardsley, R.C., Liu, H., Xu, Q., Cowles, G., 2007.
434 A finite volume numerical approach for coastal ocean circulation studies:
435 Comparisons with finite difference models. *Journal of Geophysical Research:*
436 *Oceans* 112.
- 437 Craik, A.D., Leibovich, S., 1976. A rational model for Langmuir circulations.
438 *Journal of Fluid Mechanics* 73, 401–426.
- 439 Curcic, M., 2015. Explicit air-sea momentum exchange in coupled atmosphere-
440 wave-ocean modeling of tropical cyclones. Ph.D. thesis. Citeseer.

- 441 Curcic, M., Chen, S.S., Özgökmen, T.M., 2016. Hurricane-induced ocean
442 waves and stokes drift and their impacts on surface transport and dispersion
443 in the Gulf of Mexico. *Geophysical Research Letters* 43, 2773–2781.
- 444 Curcic, M., Haus, B.K., 2020. Revised estimates of ocean surface drag in
445 strong winds. *Geophysical Research Letters* 47, e2020GL087647.
- 446 Dietrich, J., Bunya, S., Westerink, J., Ebersole, B., Smith, J., Atkinson,
447 J., Jensen, R., Resio, D., Luettich, R., Dawson, C., et al., 2010. A high-
448 resolution coupled riverine flow, tide, wind, wind wave, and storm surge
449 model for southern Louisiana and Mississippi. Part II: Synoptic description
450 and analysis of Hurricanes Katrina and Rita. *Monthly Weather Review*
451 138, 378–404.
- 452 Dietrich, J., Westerink, J., Kennedy, A., Smith, J., Jensen, R., Zijlema, M.,
453 Holthuijsen, L., Dawson, C., Luettich, R., Powell, M., et al., 2011. Hurricane
454 gustav (2008) waves and storm surge: Hindcast, synoptic analysis, and
455 validation in southern louisiana. *Monthly Weather Review* 139, 2488–2522.
- 456 Dietrich, J.C., Tanaka, S., Westerink, J.J., Dawson, C., Luettich, R., Zijlema,
457 M., Holthuijsen, L.H., Smith, J., Westerink, L., Westerink, H., 2012. Per-
458 formance of the unstructured-mesh, SWAN+ ADCIRC model in computing
459 hurricane waves and surge. *Journal of Scientific Computing* 52, 468–497.
- 460 Dobbelaere, T., Muller, E., Gramer, L., Holstein, D., Hanert, E., 2020a.
461 Report on the potential origin of the SCTLD in the Florida Reef Tract.
462 Available online at: [https://floridadep.gov/rcp/coral/documents/
463 report-potential-origin-sctld-florida-reef-tract](https://floridadep.gov/rcp/coral/documents/report-potential-origin-sctld-florida-reef-tract).
- 464 Dobbelaere, T., Muller, E.M., Gramer, L.J., Holstein, D.M., Hanert, E., 2020b.
465 Coupled epidemic-hydrodynamic modeling to understand the spread of a
466 deadly coral disease in Florida. *Frontiers in Marine Science* 7, 1016.

- 467 Donelan, M., Haus, B., Reul, N., Plant, W., Stiassnie, M., Gruber, H., Brown,
468 O., Saltzman, E., 2004. On the limiting aerodynamic roughness of the
469 ocean in very strong winds. *Geophysical Research Letters* 31.
- 470 Drivdal, M., Broström, G., Christensen, K., 2014. Wave-induced mixing and
471 transport of buoyant particles: application to the statfjord a oil spill. *Ocean*
472 *Science* 10, 977–991.
- 473 Figueiredo, J., Baird, A.H., Connolly, S.R., 2013. Synthesizing larval com-
474 petence dynamics and reef-scale retention reveals a high potential for
475 self-recruitment in corals. *Ecology* 94, 650–659.
- 476 Frys, C., Saint-Amand, A., Le Hénaff, M., Figueiredo, J., Kuba, A., Walker,
477 B., Lambrechts, J., Vallaeys, V., Vincent, D., Hanert, E., 2020. Fine-scale
478 coral connectivity pathways in the Florida Reef Tract: implications for
479 conservation and restoration. *Frontiers in Marine Science* 7, 312.
- 480 Geuzaine, C., Remacle, J.F., 2009. Gmsh: A 3-d finite element mesh generator
481 with built-in pre-and post-processing facilities. *International journal for*
482 *numerical methods in engineering* 79, 1309–1331.
- 483 Harper, B., Kepert, J., Ginger, J., 2010. Guidelines for converting between
484 various wind averaging periods in tropical cyclone conditions. *CiteSeer*.
- 485 Hegermiller, C.A., Warner, J.C., Olabarrieta, M., Sherwood, C.R., 2019.
486 Wave-current interaction between Hurricane Matthew wave fields and the
487 Gulf Stream. *Journal of Physical Oceanography* 49, 2883–2900.
- 488 Hoefel, F., Elgar, S., 2003. Wave-induced sediment transport and sandbar
489 migration. *Science* 299, 1885–1887.
- 490 Hoffmeister, J., Multer, H., 1968. Geology and origin of the Florida Keys.
491 Geological Society of America Bulletin 79, 1487–1502.

- 492 Holthuijsen, L.H., Powell, M.D., Pietrzak, J.D., 2012. Wind and waves in
493 extreme hurricanes. *Journal of Geophysical Research: Oceans* 117.
- 494 Janssen, P.A., 1991. Quasi-linear theory of wind-wave generation applied to
495 wave forecasting. *Journal of physical oceanography* 21, 1631–1642.
- 496 Johns, W.E., Schott, F., 1987. Meandering and transport variations of the
497 Florida Current. *Journal of physical oceanography* 17, 1128–1147.
- 498 Knaff, J.A., Sampson, C.R., Musgrave, K.D., 2018. Statistical tropical cyclone
499 wind radii prediction using climatology and persistence: Updates for the
500 western North Pacific. *Weather and Forecasting* 33, 1093–1098.
- 501 Knutson, T.R., McBride, J.L., Chan, J., Emanuel, K., Holland, G., Landsea,
502 C., Held, I., Kossin, J.P., Srivastava, A., Sugi, M., 2010. Tropical cyclones
503 and climate change. *Nature geoscience* 3, 157–163.
- 504 Komen, G., Hasselmann, S., Hasselmann, K., 1984. On the existence of a
505 fully developed wind-sea spectrum. *Journal of physical oceanography* 14,
506 1271–1285.
- 507 Kourafalou, V.H., Kang, H., 2012. Florida Current meandering and evo-
508 lution of cyclonic eddies along the Florida Keys Reef Tract: Are they
509 interconnected? *Journal of Geophysical Research: Oceans* 117.
- 510 Kundu, P.K., 1976. Ekman veering observed near the ocean bottom. *Journal*
511 *of Physical Oceanography* 6, 238–242.
- 512 Landsea, C.W., Franklin, J.L., 2013. Atlantic hurricane database uncertainty
513 and presentation of a new database format. *Monthly Weather Review* 141,
514 3576–3592.
- 515 Lane, E.M., Restrepo, J., McWilliams, J.C., 2007. Wave-current interaction:
516 A comparison of radiation-stress and vortex-force representations. *Journal*
517 *of physical oceanography* 37, 1122–1141.

- 518 Langmuir, I., 1938. Surface motion of water induced by wind. *Science* 87,
519 119–123.
- 520 Le Hénaff, M., Kourafalou, V.H., Paris, C.B., Helgers, J., Aman, Z.M., Hogan,
521 P.J., Srinivasan, A., 2012. Surface evolution of the Deepwater Horizon
522 oil spill patch: combined effects of circulation and wind-induced drift.
523 *Environmental science & technology* 46, 7267–7273.
- 524 Lee, T.N., Leaman, K., Williams, E., Berger, T., Atkinson, L., 1995. Florida
525 Current meanders and gyre formation in the southern Straits of Florida.
526 *Journal of Geophysical Research: Oceans* 100, 8607–8620.
- 527 Lee, T.N., Mayer, D.A., 1977. Low-frequency current variability and spin-off
528 eddies along the shelf off southeast Florida. *Collected Reprints* 1, 344.
- 529 Lee, T.N., Smith, N., 2002. Volume transport variability through the Florida
530 Keys tidal channels. *Continental Shelf Research* 22, 1361–1377.
- 531 Lee, T.N., Williams, E., 1988. Wind-forced transport fluctuations of the
532 Florida Current. *Journal of Physical Oceanography* 18, 937–946.
- 533 Li, Z., Johns, B., 1998. A three-dimensional numerical model of surface
534 waves in the surf zone and longshore current generation over a plane beach.
535 *Estuarine, Coastal and Shelf Science* 47, 395–413.
- 536 Lidz, B.H., Shinn, E.A., 1991. Paleoshorelines, reefs, and a rising sea: South
537 florida, usa. *Journal of Coastal Research* , 203–229.
- 538 Lin, N., Chavas, D., 2012. On hurricane parametric wind and applications in
539 storm surge modeling. *Journal of Geophysical Research: Atmospheres* 117.
- 540 Liu, Y., Weisberg, R.H., 2012. Seasonal variability on the West Florida shelf.
541 *Progress in Oceanography* 104, 80–98.

- 542 Liu, Y., Weisberg, R.H., Zheng, L., 2020. Impacts of hurricane Irma on the
543 circulation and transport in Florida Bay and the Charlotte Harbor estuary.
544 *Estuaries and Coasts* 43, 1194–1216.
- 545 Liubartseva, S., Coppini, G., Lecci, R., Clementi, E., 2018. Tracking plastics
546 in the Mediterranean: 2D Lagrangian model. *Marine pollution bulletin*
547 129, 151–162.
- 548 Longuet-Higgins, M.S., 1970. Longshore currents generated by obliquely
549 incident sea waves. *Journal of geophysical research* 75, 6778–6789.
- 550 Longuet-Higgins, M.S., Stewart, R., 1964. Radiation stresses in water waves;
551 a physical discussion, with applications, in: Deep sea research and oceano-
552 graphic abstracts, Elsevier. pp. 529–562.
- 553 Madsen, O.S., Poon, Y.K., Gruber, H.C., 1989. Spectral wave attenuation by
554 bottom friction: Theory, in: *Coastal Engineering 1988*, pp. 492–504.
- 555 Malmstadt, J., Scheitlin, K., Elsner, J., 2009. Florida hurricanes and damage
556 costs. *southeastern geographer* 49, 108–131.
- 557 Marsooli, R., Lin, N., Emanuel, K., Feng, K., 2019. Climate change ex-
558 acerbates hurricane flood hazards along US Atlantic and Gulf Coasts in
559 spatially varying patterns. *Nature communications* 10, 1–9.
- 560 McWILLIAMS, J.C., Restrepo, J.M., Lane, E.M., 2004. An asymptotic theory
561 for the interaction of waves and currents in coastal waters. *Journal of Fluid*
562 *Mechanics* 511, 135.
- 563 McWilliams, J.C., Sullivan, P.P., 2000. Vertical mixing by Langmuir circula-
564 tions. *Spill Science & Technology Bulletin* 6, 225–237.
- 565 Mei, C.C., 1989. The applied dynamics of ocean surface waves. volume 1.
566 World scientific.

- 567 Moon, I.J., Ginis, I., Hara, T., Thomas, B., 2007. A physics-based parameterization of air-sea momentum flux at high wind speeds and its impact on
568 hurricane intensity predictions. *Monthly weather review* 135, 2869–2878.
- 570 Pinelli, J.P., Roueche, D., Kijewski-Correa, T., Plaz, F., Prevatt, D., Zisis,
571 I., Elawady, A., Haan, F., Pei, S., Gurley, K., et al., 2018. Overview of
572 damage observed in regional construction during the passage of Hurricane
573 Irma over the State of Florida, in: *Forensic Engineering 2018: Forging
574 Forensic Frontiers*. American Society of Civil Engineers Reston, VA, pp.
575 1028–1038.
- 576 Powell, M.D., Houston, S.H., Amat, L.R., Morisseau-Leroy, N., 1998. The
577 HRD real-time hurricane wind analysis system. *Journal of Wind Engineering
578 and Industrial Aerodynamics* 77, 53–64.
- 579 Powell, M.D., Vickery, P.J., Reinhold, T.A., 2003. Reduced drag coefficient
580 for high wind speeds in tropical cyclones. *Nature* 422, 279–283.
- 581 Röhrs, J., Christensen, K.H., Hole, L.R., Broström, G., Drivdal, M., Sundby,
582 S., 2012. Observation-based evaluation of surface wave effects on currents
583 and trajectory forecasts. *Ocean Dynamics* 62, 1519–1533.
- 584 Schott, F.A., Lee, T.N., Zantopp, R., 1988. Variability of structure and
585 transport of the Florida Current in the period range of days to seasonal.
586 *Journal of Physical Oceanography* 18, 1209–1230.
- 587 Shinn, E.A., 1988. The geology of the Florida Keys. *Oceanus* 31, 46–53.
- 588 Siadatmousavi, S.M., Jose, F., Stone, G., 2011. Evaluation of two WAM
589 white capping parameterizations using parallel unstructured SWAN with
590 application to the Northern Gulf of Mexico, USA. *Applied Ocean Research*
591 33, 23–30.

- 592 Sikirić, M.D., Roland, A., Janeković, I., Tomazić, I., Kuzmić, M., 2013.
593 Coupling of the Regional Ocean Modeling System (roms) and Wind Wave
594 Model. *Ocean Modelling* 72, 59–73.
- 595 Smith, N.P., 1982. Response of Florida Atlantic shelf waters to hurricane
596 David. *Journal of Geophysical Research: Oceans* 87, 2007–2016.
- 597 Stokes, G.G., 1880. On the theory of oscillatory waves. *Transactions of the*
598 *Cambridge philosophical society* .
- 599 Tolman, H.L., et al., 2009. User manual and system documentation of
600 WAVEWATCH III TM version 3.14. Technical note, MMAB Contribution
601 276, 220.
- 602 Van Den Bremer, T., Breivik, Ø., 2018. Stokes drift. *Philosophical Trans-*
603 *actions of the Royal Society A: Mathematical, Physical and Engineering*
604 *Sciences* 376, 20170104.
- 605 Villas Bôas, A.B., Cornuelle, B.D., Mazloff, M.R., Gille, S.T., Ardhuin, F.,
606 2020. Wave–current interactions at meso-and submesoscales: Insights from
607 idealized numerical simulations. *Journal of Physical Oceanography* 50,
608 3483–3500.
- 609 Weisberg, R., Liu, Y., Mayer, D., 2009. Mean circulation on the west Florida
610 continental shelf observed with long-term moorings. *Geophys. Res. Lett*
611 36, L19610.
- 612 Weisberg, R.H., Zheng, L., 2006. Hurricane storm surge simulations for
613 Tampa Bay. *Estuaries and Coasts* 29, 899–913.
- 614 Wu, L., Chen, C., Guo, P., Shi, M., Qi, J., Ge, J., 2011. A FVCOM-
615 based unstructured grid wave, current, sediment transport model, I. Model
616 description and validation. *Journal of Ocean University of China* 10, 1–8.

- 617 Xian, S., Feng, K., Lin, N., Marsooli, R., Chavas, D., Chen, J., Hatzikyriakou,
618 A., 2018. Brief communication: Rapid assessment of damaged residential
619 buildings in the Florida Keys after Hurricane Irma. *Natural Hazards and*
620 *Earth System Sciences* 18, 2041–2045.
- 621 Zedler, S., Niiler, P., Stammer, D., Terrill, E., Morzel, J., 2009. Ocean's
622 response to Hurricane Frances and its implications for drag coefficient
623 parameterization at high wind speeds. *Journal of Geophysical Research: Oceans* 114.
- 625 Zhang, C., Durgan, S.D., Lagomasino, D., 2019. Modeling risk of mangroves
626 to tropical cyclones: A case study of Hurricane Irma. *Estuarine, Coastal*
627 *and Shelf Science* 224, 108–116.